

See discussions, stats, and author profiles for this publication at: <https://www.researchgate.net/publication/231660300>

# Pore Structure Characterization of Mesoporous/Microporous Materials by $^1\text{H}$ NMR Using Water as a Probe Molecule

ARTICLE in THE JOURNAL OF PHYSICAL CHEMISTRY B · DECEMBER 1997

Impact Factor: 3.3 · DOI: 10.1021/jp9721964

CITATIONS

31

READS

35

3 AUTHORS, INCLUDING:



Eddy Walther. Hansen

University of Oslo

112 PUBLICATIONS 1,475 CITATIONS

SEE PROFILE



Elisabeth Tangstad

SINTEF

18 PUBLICATIONS 283 CITATIONS

SEE PROFILE

# Pore Structure Characterization of Mesoporous/Microporous Materials by $^1\text{H}$ NMR Using Water as a Probe Molecule

Eddy Walther Hansen,\* Elisabeth Tangstad, and Elisabeth Myrvold

SINTEF Applied Chemistry, P.O. Box 124, Blindern, N-0314 Oslo, Norway

Trond Myrstad

Statoil R&D Centre Postuttak, N-7005 Trondheim, Norway

Received: July 7, 1997; In Final Form: August 24, 1997<sup>®</sup>

Model improvements related to the analysis of  $^1\text{H}$  NMR signal intensity vs temperature (IT-curve) of a fluid confined in porous materials are presented enabling pore size distribution, specific surface area, and relative distribution of pore volumes to be extracted. The model is applied to four different porous materials, two containing mesopores only and two containing both mesopores and micropores.

## Introduction

In a series of articles Hansen and co-workers<sup>1–6</sup> have shown how high-resolution  $^1\text{H}$  NMR can be used to characterize the porous network of mesoporous materials by using water as a probe molecule. The technique is based on monitoring the amount of solid ice being melted vs temperature below the normal melting point of bulk solid ice. These intensity vs temperature curves (IT-curves) represent unique model independent fingerprints of the porous network. In combination with theoretical modeling, they have been able to transform these IT-curves into pore size distributions.

In this work, we will present improvements in the theoretical model used to derive pore size distribution. In particular, the modified theoretical model will be used to fit IT-curves of two (or more) samples simultaneously in order to constrain the fitting more effectively. Moreover, this procedure will enable model parameters to be derived from NMR measurements alone without the need to combine other experimental techniques ( $\text{N}_2$ -adsorption). This approach will be exemplified using two commercial, mesoporous ( $500 \text{ \AA} > R \geq 10 \text{ \AA}$ ) silica samples. The derived pore size distributions will be compared to the corresponding pore size distributions obtained by independent  $\text{N}_2$ -adsorption measurements.

Of particular novelty, two, noncommercial samples containing both micropores ( $R \leq 10 \text{ \AA}$ ) and mesopores will be investigated to see whether the relative amount of micropores can be extracted from such NMR measurements. Also, the possibility of obtaining specific surface area of porous materials will be discussed and compared with  $\text{N}_2$  adsorption measurements.

## Experimental Section

The four porous materials investigated in this work were two commercial Kiselgels of types "40 and 60" from Merck with nominal pore diameters of 40 and 60  $\text{\AA}$ , respectively. In the following discussion these materials will be denoted S40 and S60. The two other samples were noncommercial materials containing both mesopores and micropores (zeolite) and are denoted A and B, respectively.

All samples were dried for 24 h at a temperature of 403 K in a conventional oven before being saturated with water under

vacuum and subsequently supersaturated with water to ensure that all pore space was filled with water.

The samples were characterized by  $\text{N}_2$  adsorption in order to compare the consistency in pore size distribution obtained by NMR and  $\text{N}_2$  adsorption. The water-saturated samples were studied by  $^1\text{H}$  NMR at subzero temperature ( $T < 273 \text{ K}$ ) using a Varian VXR NMR spectrometer, operating at 300 MHz proton resonance frequency. The accuracy of the temperature determination was  $\pm 0.5 \text{ K}$ . A bandwidth of 100 kHz, an acquisition time of 0.025 s, and a  $90^\circ$  pulse of  $15 \mu\text{s}$  were applied with a repetition time of 15 s between the radio-frequency pulses. Each spectrum was composed of four transients. The long interpulse timing was dictated by the long spin–lattice relaxation time of potential silanol protons, which exhibits spin–lattice relaxation times of approximately 3–4 s.<sup>6,7</sup> The free induction decay (FID) was sampled after blanking the receiver for  $20 \mu\text{s}$ , thus enabling the signal from the solid ice phase to be ignored because of its very short spin–spin relaxation rate in the range of a few microseconds. Moreover, due to the extremely long spin–lattice relaxation time ( $T_1$ ) of the water protons of solid ice at this high magnetic field strength ( $T_1 \approx 900 \text{ s}$  at 263 K and 7.05 T)<sup>8,9</sup> any residual signal from the solid ice phase would be significantly reduced when taking into account the relatively short pulse repetition time of 15 s used in this work. The temperature was changed in steps of 1 K. A temperature equilibration of 1 min was applied before any measurement was initiated. This seemingly short equilibration time has been previously shown (unpublished) to give NMR signal intensities which do not differ significantly from NMR signal intensities measured after 5–10 min of temperature equilibration. The intensity was determined by numerical integration of the resonance peak and corrected for temperature according to Curie's law;<sup>10</sup> i.e., the NMR signal intensity measured at a temperature  $T$  was corrected by multiplication by the factor  $T/T_0$ , with  $T_0 = 273.15 \text{ K}$ . The  $^1\text{H}$  NMR IT-curve was obtained by slowly cooling the sample to 173 K and then heating the sample to 278 K while recording the different NMR spectra.

## Theoretical Concept

The basic theory and concept involved in deriving pore size distributions of porous materials from  $^1\text{H}$  NMR IT-curves has been discussed elsewhere<sup>1–6</sup> and will only briefly be summarized in this section.

\* To whom correspondence should be addressed.

<sup>®</sup> Abstract published in *Advance ACS Abstracts*, November 15, 1997.

A combined use of NMR and  $N_2$ -adsorption has shown that the relation between pore radius ( $R$ ) and transition temperature ( $T_c$ ) can be described by a modified Gibbs–Thompson equation<sup>11,12</sup> of the form

$$\Delta T = T_0 - T_c = \frac{K}{R_c - d} \quad (1)$$

where  $\Delta T$  represents the melting point depression, i.e., the difference between the bulk melting point ( $T_0$ ) and the actual observed melting point ( $T_c$ ) of the solid confined in a pore of dimension  $R$  (average pore radius).  $K$  and  $d$  are constants which are dependent on the actual probe molecule (solid) used. The parameter  $d$  represents the thickness of an interface layer (between the matrix and the solid ice within the pore) which melts at a lower temperature than the rest of the solid ice within the pore. The melting point depression ( $\Delta T$ ) in eq 1 can be determined from the observed  $^1\text{H}$  NMR IT-curve by fitting the model equation (eq 2) to the experimental IT-curve

$$I(X) = \sum_{i=1}^N \frac{I_{0i}}{\sqrt{\pi}} \int_{-\infty}^{(X - X_{ci})/\sqrt{2\Delta_i}} \exp(-u^2) du \quad (2)$$

where  $X$  represents the inverse absolute temperature ( $X = 1000/T$ ). Equation 2 thus represents the amount of fluid, i.e., the total amount of solid which has been melted within the pores at temperature  $X$  ( $=1000/T$ ). If differentiating eq 2 with respect to  $X$ , the “melting point” distribution curve ( $dI/dX$ ) is obtained and is represented by a simple sum of Gaussian functions centered around  $X_{ci}$  with half-width  $\Delta_i$ , (eq 3):

$$\frac{dI}{dX} = \sum_{i=1}^N \frac{I_{0i}}{\sqrt{2\pi}\Delta_i} \exp\left[-\left(\frac{X - X_{ci}}{\sqrt{2\Delta_i}}\right)^2\right] \quad (3)$$

The pore size distribution ( $dI/dR$ ) can easily be derived from the melting-point distribution curve ( $dI/dX$ ; eq 3) by noting that  $dI/dR = dI/dX \cdot dX/dR$ . The term  $dX/dR$  can be found from eq 1 and results in the following equation for the pore size distribution:

$$\frac{dI}{dR} = \frac{1}{10^3 K} \sum_{i=1}^N \frac{I_{0i}}{\Delta_i \sqrt{2\pi}} (XT_0 - 10^3)^2 \cdot \exp\left[-\left(\frac{X - X_{ci}}{\sqrt{2\Delta_i}}\right)^2\right] \quad (4)$$

Equation 4 suggests that if a material is characterized by  $(N - 1)$  discrete pore sizes a corresponding number  $(N - 1)$  of temperature transitions will be observed. However, all materials investigated in this laboratory reveal  $N$  transitions. Even well characterized MCM-41 materials having only a single pore dimension (XRD) reveal two temperature transitions where the lower transition cannot be explained by eq 1. These observations suggest<sup>4</sup> that the lowest temperature transition ( $i = N$ ) observed by the present NMR technique cannot be related to the melting of solid confined in a pore having a well-defined and single pore dimension. We have suggested that this transition is related to the melting of an “interface layer” located between the pore surface matrix and the rest of the pore solid and having a thickness  $d$ . Whether the parameter  $d$  is constant and independent of the “roughness” of the pore surface is unclear. However, recently published data indicate that—within experimental error—the variation in  $d$  vs type of material is only marginal.<sup>5</sup>  $d$  will thus be treated as a constant in this work.

This “interface layer” transition has in previous publications been excluded from eq 4 when deriving pore size distributions

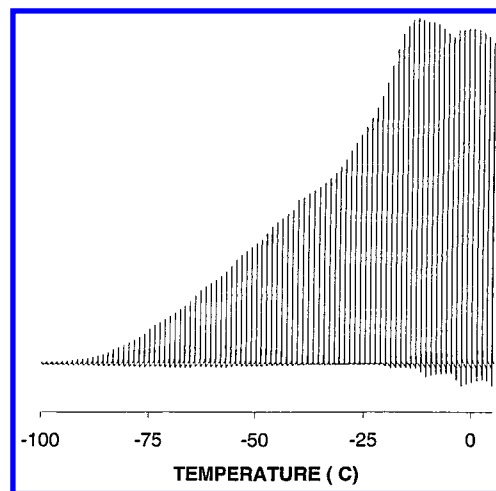


**Figure 1.** Experimental  $^1\text{H}$  NMR spectra of water confined in samples S40 during heating of the sample from 100 to  $+5$   $^{\circ}\text{C}$ . Each line represents the actual  $^1\text{H}$  NMR spectrum at the specified temperature.

and leads to a truncated pore size distribution. An important object in this work is to modify eq 2 in order to take account of this subtle anomaly.

## Results and Discussion

**A. IT-Curves and Melting Point Distribution Curves—Model Improvements.** Figure 1 shows successive  $^1\text{H}$  NMR spectra vs temperature of water-saturated silica (S40) during heating from  $-100$  to  $+5$   $^{\circ}\text{C}$ . The reason for not running a cooling experiment is that the transition temperature will be located at a lower temperature compared to the transition temperature observed in a heating experiment. This is mainly caused by supercooling of the confined fluid during freezing and results in characteristic hysteresis effect.<sup>4</sup> Thus, from previous measurements we simply conclude that the melting point transition represents a better description of the apparent phase transition as compared to the observed freezing point transition. As can be seen from Figure 1 a distinct transition in intensity vs temperature during heating can be inferred at approximately  $-15$   $^{\circ}\text{C}$  which is due to melting of water within pores of a specific radius  $R$  as given by eq 1.

The numerical value of the intensity (area) of each resonance peak vs inverse absolute temperature (IT-curve) of samples S40 and S60 is shown in Figure 2 where the solid curves represent model fits to eq 2. The derived transition temperature ( $T_{ci}$ ), the width ( $\Delta_i$ ), and the corresponding intensity ( $I_{0i}$ ) of each transition ( $i$ ) are summarized in Table 1. The lower part of Figure 2 shows the residuals, i.e., the difference between observed and model-fitted intensities (eq 2) vs inverse absolute temperature for both samples and suggests that the residuals are randomly distributed. We have not made any distinction between samples S40 and S60 in this figure because there was no observable difference in residuals between the two samples.

The optimum number of components needed to fit each observed IT-curve was determined by statistical validity tests ( $F$ -test) and resulted in four extractable transitions for each sample. The reason for presenting the residuals will become clear later.

The abrupt decrease in temperature close to the melting point of bulk water of sample S60 represents the melting of intercrystalline water. No such intercrystalline water could be observed in sample S40, due to an accidental initial temperature exposure at  $+80$   $^{\circ}\text{C}$  for a very short period of time (resulting in the removal of practically all intercrystalline water). That

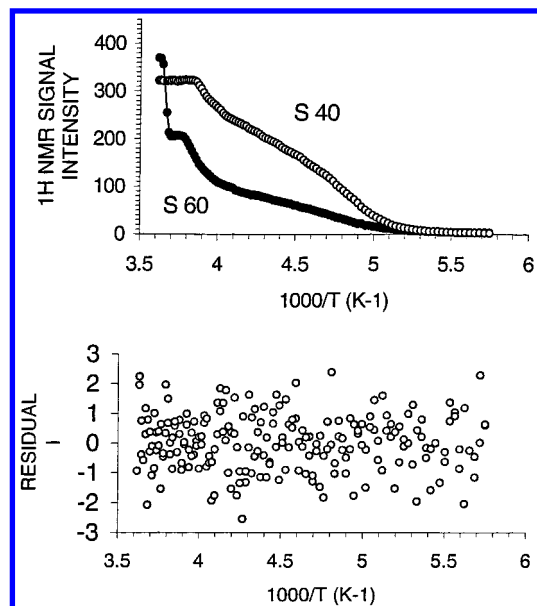


**Figure 2.** (Top) Numerical  $^1\text{H}$  NMR signal intensity vs inverse absolute temperature of water confined in samples S40 and S60 during melting. Solid curves represent model fits to eq 2. (Bottom) Residual signal intensity between observed and fitted IT-curves of samples S40 and S60 vs temperature. The ordinates of the top and bottom parts are the same.

**TABLE 1: Intensity ( $I_{0i}$ ), Melting Temperature  $T_{ci}$ , and Width ( $\Delta T_{ci}$ ) of the Individual Temperature Transitions ( $i$ ) Obtained by Fitting the Observed IT-Curve to Two Different Models: A (Eq 2) and B (Eq 6), Respectively**

parameter	S60 (A)	S60 (B)	S40 (A)	S40 (B)
$I_{01}$	$53 \pm 15$	$67 \pm 8$	$33 \pm 5$	$57 \pm 7$
$T_{01}(\text{K})$	$261.1 \pm 0.2$	$261.1 \pm 0.2$	$256.7 \pm 0.2$	$256.6 \pm 0.2$
$\Delta_1(\text{K})$	$2.3 \pm 0.2$	$2.3 \pm 0.2$	$1.7 \pm 0.2$	$2.2 \pm 0.2$
$I_{02}$	$50 \pm 18$	$51 \pm 7$	$38 \pm 7$	$79 \pm 11$
$T_{02}(\text{K})$	$254.3 \pm 1.2$	$255.4 \pm 0.7$	$250.0 \pm 0.7$	$249.8 \pm 0.6$
$\Delta_2(\text{K})$	$3.9 \pm 1.3$	$3.1 \pm 0.5$	$3.3 \pm 0.6$	$3.5 \pm 0.6$
$I_{03}$	$22 \pm 7$	$85 \pm 5$	$78 \pm 8$	$182 \pm 5$
$T_{03}(\text{K})$	$249.3 \pm 1.9$	$249.3 \pm 0.6$	$234.6 \pm 0.6$	$234.3 \pm 0.4$
$\Delta_3(\text{K})$	$5.3 \pm 1.4$	$8.9 \pm 0.1$	$9.6 \pm 0.8$	$8.2 \pm 0.3$
$I_{04}$	$78 \pm 3$		$170 \pm 4$	
$X_{04}(\text{K})$	$213.3 \pm 0.6$		$207.7 \pm 0.3$	
$\Delta_4(\text{K})$	$12.3 \pm 0.5$		$9.5 \pm 0.2$	

no intracrystalline water had been removed during the “high” temperature exposure was confirmed later. For completeness, the temperature distribution curves,  $dI/dX$  (eq 3), are plotted in Figure 3 and show rather broad melting transitions in the low-temperature region of the spectrum, at approximately 210 K. As pointed out in the previous section, this low-temperature transition ( $N = 4$ ) represents the melting of an interface layer located between the matrix and the rest of the solid ice within the pore. This formation of a liquid interface layer does not reveal any characteristic hysteresis effect.<sup>4</sup> The temperature distribution curve represents an alternative fingerprint of the porous network and is completely independent of any assumptions regarding pore geometry. Note that the intensity of this broad transition is significantly larger for sample S40 compared to sample S60. The reason for this larger fraction of interface water in the former sample is ascribed to its smaller pore dimension, i.e., the interface water constitutes a larger amount of water compared to the residual pore water in this sample.

If the pore geometry is known, the amount of interface water can be expressed analytically. For instance, if the pores can be represented by infinitely long cylinders or spheres with radius  $R$ , the volume fraction ( $F$ ) of interface water can be expressed by

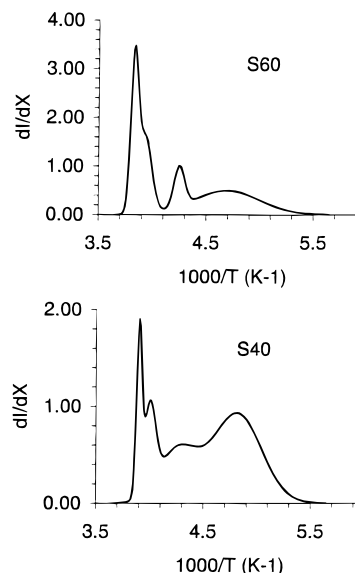


**Figure 3.** Melting distribution curves of water confined in samples S60 (top) and S40 (bottom) as derived from eq 3.

$$F(R) = \frac{V_{\text{int}}}{V_T} = 1 - \left(1 - \frac{d}{R}\right)^\alpha \quad (5a)$$

where  $\alpha$  is equal to 3 for spherical pores and equal to 2 for cylindrical pores.  $V_q$  represents the amount of interface water ( $q = \text{int}$ ) and the total amount of pore water ( $q = T$ ), respectively,  $d$  is the thickness of the interface or surface layer. The pore radius ( $R$ ) can be related to temperature via eq 1, implying that  $F$  can be expressed by the inverse absolute temperature  $X (= 1000/T)$  rather than the pore radius, i.e.

$$F(X) = 1 - \left[1 + \frac{10^3 d}{K} \left(\frac{1}{X_0} - \frac{1}{X}\right)\right]^{-\alpha} \quad (5b)$$

Regardless of the pore dimension (mesopores), all pores will have a surface layer which melts at a lower temperature than the rest of the pore solid. Since the thickness of this surface layer is assumed to be constant and equal to  $d$ , we will assume that it will melt at a temperature ( $T_s$ ) which is independent of the actual pore dimension. Thus, eq 2 can be reformulated to give

$$I(X) = \sum_{i=1}^{N-1} \frac{I_{0i}^*}{\sqrt{\pi}} [1 - F(X_{ci})] \cdot \int_{-\infty}^{(X-X_{ci})/\sqrt{2\Delta_i}} \exp(-u^2) du + \sum_{i=1}^{N-1} F(X_{ci}) \cdot \int_{-\infty}^{(X-X_s)/\sqrt{2\Delta_s}} \exp(-u^2) du \quad (6)$$

The second term in eq 6 corresponds to the  $N$ th term in eq 2 and leads to an additional constraint when used in model fitting. Of particular importance is that when fitting eq 6 to the observed IT-curve, the “true” amount of water ( $I_{0i}^*$ ) or “true” pore volumes will be obtained which is in contrast to eq 2 which only gives the amount ( $I_{0i}$ ) of “bulk” water within the pores, i.e., the pore volume minus the volume of the interface layer. This effect might have a significant impact on the shape of the derived pore size distribution and will be discussed in the next section. Equation 6 represents so far a final theoretical expression for the IT-curve or more roughly, the “melting point curve”. Further improvement of this model equation will involve the possible temperature dependence of the parameter

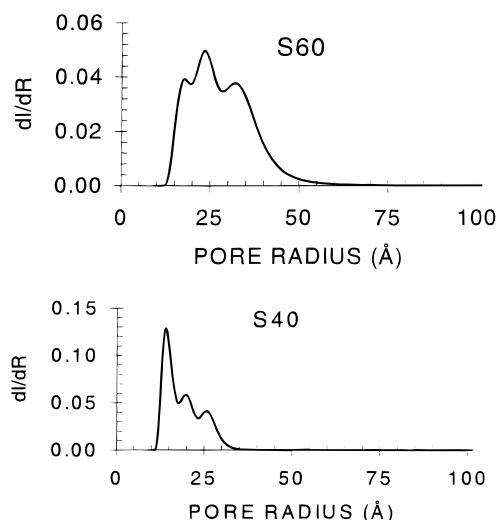


**Figure 4.** Normalized pore size distribution curves (eq 4) derived by parameter input from fitting observed IT-curves to eq 6 for samples S60 (top) and S40 (bottom).

$K$  (due to its dependence on heat of fusion and surface tension) which will be a subject for future studies.

**B. Pore Size Distribution.** When using eq 6 to derive the pore size distribution, the parameters  $K$  and  $d$  and the pore volume intensities ( $I_i^*$ ) are needed. These intensity parameters can be determined by fitting the observed IT-curves to eq 6 if knowing the two former parameters are known. These parameters ( $K$  and  $d$ ) have been estimated and published in a previous paper<sup>5</sup> by combining NMR and  $N_2$ -adsorption experiments. However, in this work we will determine these parameters from NMR measurements alone by applying only the model equation represented by eq 6 (and eq 5b) on two different samples simultaneously.

The experimental IT-curves of samples S40 and S60 have been fitted simultaneously to eq 6 by a nonlinear least-squares fit using a simplex algorithm under the constraint that  $K$  and  $d$  are the same in both samples. This is equivalent of solving a set of 200 equations with 20 unknowns. The previously derived  $T_{ci}$ ,  $\Delta_i$ , and  $I_{oi}$  values (Table 1) from eq 2 (Table 1) were used as initial input values in the fit. The final results of the fit are summarized in Table 1 and show that the transition temperatures and width parameters are—within experimental uncertainty—the same as derived by fitting eq 2 to the observed IT-curves. However, the intensity parameters have become larger; i.e., the difference between  $I_{oi}^*$  and  $I_{oi}$  increases with decreasing transition temperature due to the effect of the existence of an interface layer (of constant thickness) as discussed in the previous section. For instance, the intensity of the lowest transition temperature of samples S40 and S60 have increased by more than a factor of 2 and 4, respectively.

The uncertainty in the derived parameters (Table 1) were estimated as follows; Since the residuals between the observed and fitted IT-curves are seen to be approximately randomly distributed (lower part of Figure 2), five synthetic IT-curves were generated randomly within the estimated 99% confidence interval (lower part of Figure 2). A nonlinear least-squares fit—as just outlined—was performed on each of the five synthetic data sets, and the average value and corresponding standard deviation of each parameter were determined by standard statistical procedures. The derived values of  $K$  and  $d$  were found to be  $K = (355 \pm 17) \text{ K} \cdot \text{\AA}$  and  $d = (5.9 \pm 0.3) \text{ \AA}$ , respectively, and are somewhat different from previous findings<sup>5</sup> ( $K = 515 \text{ K} \cdot \text{\AA}$  and  $d = 3.6 \text{ \AA}$ ). We have used this value of  $K$  to generate the pore size distributions (Figure 4) which can be compared

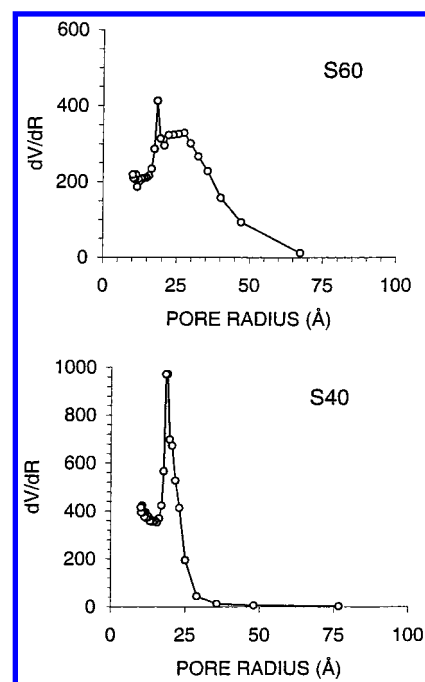


**Figure 5.** Pore size distribution curves of samples S60 (top) and S40 (bottom) derived from  $N_2$ -adsorption measurements.

**TABLE 2: Pore Radii ( $R_{oi}$ , Assuming Cylindrical Pores) and Relative Pore Volumes ( $V_{oi}$ ) of Samples S40, S60 As Derived from Eqs 6–8**

parameter	S60	S40
$R_{01} (\text{\AA}) // V_{01} (\%)$	35.8 // 33	26.9 // 57
$R_{02} (\text{\AA}) // V_{02} (\%)$	25.9 // 25	21.4 // 25
$R_{03} (\text{\AA}) // V_{03} (\%)$	25.2 // 42	15.6 // 18
$R_{av} (\text{\AA}; \text{NMR})$	28.9	19.0
$R_{av} (\text{\AA}; N_2\text{-ads})$	25	19

with the corresponding pore size distributions obtained by  $N_2$ -adsorption measurements (Figure 5). The resemblance is rather striking. NMR seems, however, to give a far better resolution than  $N_2$ -adsorption. To obtain a better quantitative comparison we have calculated the average pore dimension of each pore size distribution by applying eq 7;

$$R_{av} = \int_0^\infty R \cdot \left[ \frac{dI}{dR} \right] dR / \int_0^\infty \left[ \frac{dI}{dR} \right] dR \quad (7)$$

The results are summarized in Table 2 and show an excellent agreement between the two independent techniques for sample S40. As to the S60 sample, NMR predicts a 15% larger value for  $R_{av}$  compared to the corresponding average pore dimension derived from  $N_2$ -adsorption. The uncertainty in the derived average pore dimension from  $N_2$ -adsorption is, however, probably high due to the poorer resolution and the ill-defined behavior of the distribution for smaller pore radii. The corresponding uncertainty in pore dimension derived from NMR measurements is estimated to be less than approximately 2%. Also included in Table 2 are the average pore dimensions and volume contributions of each resolved peak in the NMR spectrum. In short, we can conclude that the two different techniques give rather similar predictions of the pore size distributions of the two reference samples.

An important consequence of the results obtained by NMR is that eq 1 has no physical significance for pore radii smaller than  $d$  ( $=5.9 \text{ \AA}$ ), i.e., in the range of micropores. This means that the correlation between melting point and pore radius of micropores must have a different functional form than predicted by eq 1. This is supported by a few measurements reported on



water-saturated zeolite- $\beta$ ,<sup>13</sup> which has a pore dimension in the range of  $d$ . This zeolite material reveals a melting point close to 203 K, depending somewhat on the Si/Al-ratio. The correlation between melting point and pore dimension of water confined in micropores remains thus unknown. Whether a such a correlation exists or not remains unanswered, but it is an interesting and basic topic of more fundamental importance and suggests that when approaching the dimension of micropores, the thermodynamic/macrosopic concept of freezing/melting breaks down.

One should also recall that the parameter  $K$  (in eq 1) will be dependent on the type of solid being used as probe molecule, since  $K$  is related to properties such as melting enthalpy, density, and surface tension. Our experience with the present NMR technique suggests, however, that for a specific choice of probe molecule  $K$  is not very sensitive to the chemical nature of the porous material. It should be emphasized, however, that—to our knowledge—no systematic investigation regarding the chemical nature of the porous surface and its effect on  $K$  has been reported, and therefore needs to be addressed.

Another point of concern relates to the potential temperature dependence of  $K$  since  $K$  is a function of surface tension and melting enthalpy which are known to be temperature dependent. The reason for not observing any such temperature effect in  $K$  may be accidental; i.e., it might be that the temperature dependence of surface tension and enthalpy of melting partly cancel each other. This needs further investigation.

Another important consequence of the present discussion is that there must exist a certain pore dimension at which no macroscopic “bulk” melting of ice takes place. For instance, since the surface thickness or interface thickness of the water layer is determined to be 5.9 Å, no pure “bulk” water phase is expected to exist at or below this pore dimension. This suggests that there must exist a critical temperature ( $X_{\text{crit}}$ ) where the fraction of observable “bulk” water approaches zero, i.e.,  $F(X < X_{\text{crit}}) = 1$ . We have seen that for water confined in zeolite- $\beta$ , the melting temperature is approximately 203 K. Since this water—according to the concept applied in this work—must be identified as interface water or surface water,  $F(X=1000/203)$  should be equal to 1. Using eq 5b, we obtain, however,  $F = 0.79$  at this temperature, which is significantly smaller than 1 and suggests breakdown of eq 1 for pore sizes in the microporous range.

The distinct separation of bulk and interface water seen in the temperature distribution curves (Figure 3) suggests that the specific surface area,  $\hat{S}_p$ , can be estimated from these NMR measurements via eq 3 if knowing the specific pore volume,  $\hat{V}_p$ .

$$\frac{I_N}{\sum_{i=1}^N I_i} = \frac{I_N}{I_T} = \frac{S_p \cdot d}{V_p} = \frac{S_p/m_s}{V_p/m_s} \cdot d = \frac{\hat{S}_p}{\hat{V}_p} \cdot d \quad (8)$$

All parameters in eq 8 have previously been defined except for  $S_p$ ,  $V_p$ , and  $m_s$ , which represent the total pore surface area, the total pore volume, and the weight of dry material, respectively.

The specific pore volume,  $\hat{V}_p$ , was determined from the known amount of water added to the material in combination with the observed IT-curve. The resulting specific surface area was estimated from eq 8. The results are summarized in Table 3. Considering the experimental uncertainties, good agreement between NMR and  $\text{N}_2$ -adsorption measurements is found.

The accuracy of the derived specific surface area from eq 8 is dependent on how well the surface thickness ( $d$ ) can be

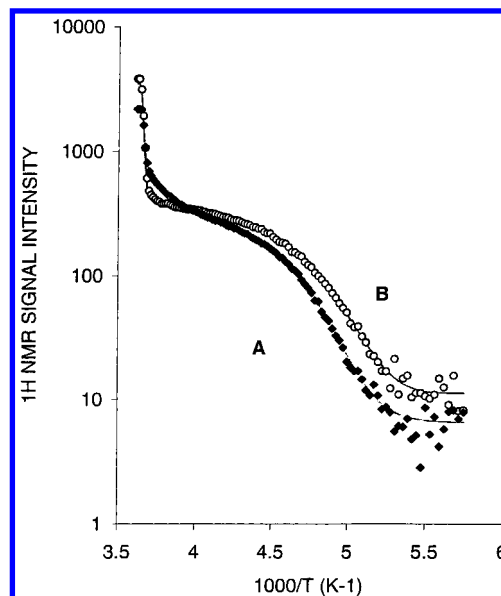


**Figure 6.** (Top) Numerical  $^1\text{H}$  NMR signal intensity vs inverse absolute temperature of water confined in samples A and B during melting. Solid curves represent model fits to eq 6 (+ eq 9).

**TABLE 3: Specific Surface Area Obtained from NMR and  $\text{N}_2$ -Adsorption Measurements**

sample	$S$ ( $\text{m}^2/\text{g}$ ) (NMR)	$S$ ( $\text{m}^2/\text{g}$ ) ( $\text{N}_2$ -ads)
S40	$746 \pm 37$	770
S60	$551 \pm 28$	475
A	$236 \pm 2$	269
B	$132 \pm 1$	214

estimated. As previously discussed, this parameter is calculated by assuming cylindrical pore geometry. Assuming the pore geometry to be purely spherical, the calculated  $d$ -value will become systematically larger by approximately 20%.<sup>5</sup> At present, the NMR technique cannot give information regarding the actual or true pore geometry. However, an assumption regarding pore geometry must be decided upon before fitting the actual model to the observed NMR data. In consistency with  $\text{N}_2$ -adsorption measurements we have—in this work—assumed cylindrical pore geometry.

**C. Porous Materials Containing Micropores.** Figure 6 shows the IT-curves of samples A and B. The corresponding melting-point distribution curves are depicted in Figure 7 and are derived as discussed in the previous section, i.e., fitting the observed IT-curve to eq 2 and inserting the fitted parameters into eq 3. Characteristic broad peaks at low temperature ( $T < 230$  K) are observed in both samples during heating (Figure 7) and are characteristic of melting of interface water and/or melting of water confined in micropores. To enable a quantitative separation of interface water and microporous water we have simply added an extra term,  $I_z(X)$  in eq 6 which has the same functional form as the interface water transition, i.e.

$$I_z(X) = \frac{I_{0z}}{\sqrt{\pi}} \int_{-\infty}^{(X-X_z)/\sqrt{2}\Delta_s} \exp(-u^2) du \quad (9)$$

The solid curves in Figure 6 represent model fits to eq 6 including the microporous term (eq 9). The relative amount of microporous volume determined by this fit was found to be  $(14.8 \pm 1.3)\%$  for sample A and  $(24.9 \pm 0.5)\%$  for sample B. These numbers should be compared with the corresponding wt % numbers derived from  $\text{N}_2$ -adsorption measurements of 15.2% and 26.4%, respectively. Assuming the mesoporous and microporous part of the material to have approximately the same

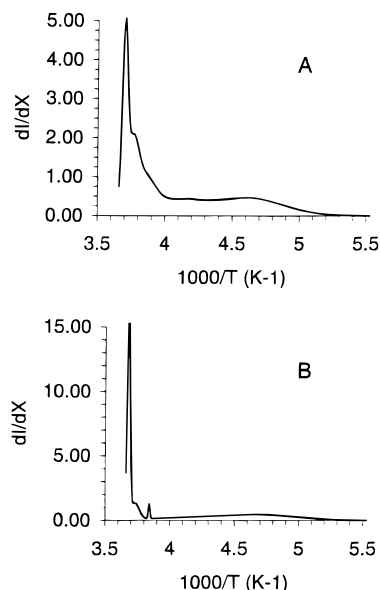


**Figure 7.** Melting distribution curves of water confined in samples A (top) and B (bottom) as derived from eq 3.

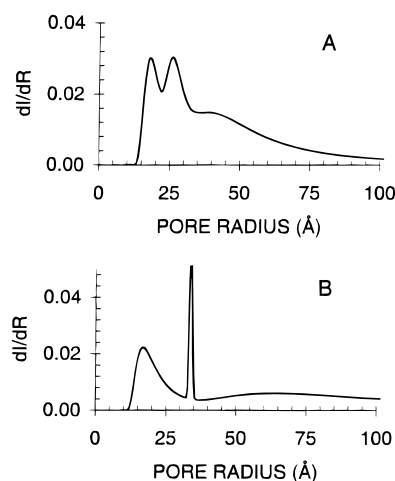


**Figure 8.** Normalized pore size distribution curves (eq 4) derived by parameter input from fitting observed IT-curves to eq 6 (+ eq 9) for samples A (top) and B (bottom).

densities, these numbers are—within experimental error—identical, suggesting that the NMR technique can be used to determine the relative amount of micropores in the sample. The temperature transition of the interface water was the same for all samples ( $210 \pm 4$ ) K except for sample A which showed a transition at 230 K. However, the half-width of the temperature transition was approximately 12 K for all four samples. The reason for the significantly higher temperature transition observed for the interface water in sample A is not known. We noted, however, that when fitting eq 6 (+ eq 9) to the observed IT-curve of sample A, the convergence was somewhat unstable, i.e., it depended on the initial choice of starting parameters in the iteration process.

The observed transition temperature of water confined in the micropores of samples A and B was approximately the same (215 K) with a significantly broad temperature distribution of the transition of approximately 17 K (half-width of the distribution). Interesting is the observation that the derived transition

temperature of interface water and water confined in microporous are nearly the same.

The resulting (meso)pore size distributions—as derived from eq 4—are shown in Figure 8 and are in qualitative agreement with corresponding distribution curves obtained by  $N_2$ -adsorption measurements (not shown).

Also, the specific surface area of samples A and B was estimated from eq 8. The results are summarized in Table 3 and reveal a significant difference in specific surface area of sample B when comparing  $N_2$ -adsorption and NMR measurements. This difference might originate from the implicit assumption of the existence of an interface layer of water molecules (between the matrix surface and solid ice within the pore) of thickness  $d$  (6 Å). This assumption is certainly not valid for pores of dimension smaller than  $d$ .

Moreover, the amount of fluid molecules that can enter the micropores will be dependent on the adsorption characteristics of the fluid–zeolite system; i.e., the amount of adsorbed fluid will be a function of the Si/Al-ratio<sup>13</sup> and the choice of probe molecule  $a$ . This might affect the estimate of both surface area and pore volume of the micropores. These factors must be investigated in order to validate the applicability of the present NMR technique to estimate specific surface area and relative amount of micropores within microporous materials. Other probe molecules than water might be used with advantage and will be the subject for future work.

## Conclusion

Analysis of the  $^1H$  NMR signal intensity of water confined in mesoporous materials during heating enables the pore size distribution and specific surface area of the materials to be extracted. The relevant model equations used to derive these parameters are discussed and permit a detailed quantitative characterization of the porous network. Preliminary application of this NMR technique to materials containing both mesopores and micropores suggests that the technique can be applied to discriminate between mesopores and micropores. However, establishing the exact pore size distribution of micropores within a material needs further and more basic investigation.

## References and Notes

- (1) Hansen, E. W.; Schmidt, R.; Stöcker, M.; Akporiaye, D. *J. Phys. Chem.* **1995**, *99*, 4148–4154.
- (2) Schmidt, R.; Hansen, E. W.; Stöcker, M.; Akporiaye, D.; Ellestad, O. H. *J. Am. Chem. Soc.* **1995**, *117*, 4049–4056.
- (3) Schmidt, R.; Stöcker, M.; Hansen, E. W.; Akporiaye, D.; Ellestad, O. H. *Microporous Mater.* **1995**, *3*, 443–448.
- (4) Akporiaye, D.; Hansen, E. W.; Schmidt, R.; Stöcker, M. *J. Phys. Chem.* **1993**, *97*, 7743.
- (5) Hansen, E. W.; Stöcker, M.; Schmidt, R. *J. Phys. Chem.* **1996**, *100*, 11396–11401.
- (6) Hansen, E. W.; Stöcker, M.; Schmidt, R. *J. Phys. Chem.* **1996**, *100*, 2195–2200.
- (7) Overloop, K.; Van Gerven, L. *J. Magn. Reson. Ser. A* **1993**, *101*, 179.
- (8) Barnaal, D. E.; Lowe, I. J. *J. Chem. Phys.* **1967**, *48*, 4614.
- (9) Barnaal, D. E.; Kopp, M.; Lowe, I. J. *J. Chem. Phys.* **1976**, *65*, 5495.
- (10) Abragam, A. *The Principles of Nuclear Magnetism*; Clarendon Press: Oxford, U.K., 1961.
- (11) Gibbs, J. W. *The Collected Works of J. Willard Gibbs*; Academic Press: New York, 1928.
- (12) Thompson, W. (Lord Kelvin). *Philos. Mag.* **1871**, *42*, 448–45213.

Hansen, E. W.; Iding, M.; Lillerud, K-P.; Stöcker, M. Submitted to *Solid State Nucl. Magn. Reson.*